

The connectome predicts resting-state functional connectivity across the *Drosophila* brain

Highlights

- Functional correlations are predicted by structural connectivity in the connectome
- Correlations are well captured by the number of cells connecting two regions
- Mesoscale networks in the *Drosophila* brain share topological features with cortex
- Indirect pathways differentially shape functional correlations across the brain

Authors

Maxwell H. Turner, Kevin Mann,
Thomas R. Clandinin

Correspondence

trc@stanford.edu

In brief

Turner et al. use the central brain connectome of the fruit fly *Drosophila* to show how structural connectivity between brain regions can predict functional correlations measured using *in vivo* brain imaging. The authors show that brain networks in *Drosophila* share topological features with mammalian cortical networks.



Report

The connectome predicts resting-state functional connectivity across the *Drosophila* brain

Maxwell H. Turner,^{1,2} Kevin Mann,^{1,2} and Thomas R. Clandinin^{1,3,*}

¹Department of Neurobiology, Stanford University, Stanford, CA 94103, USA

²These authors contributed equally

³Lead contact

*Correspondence: trc@stanford.edu

<https://doi.org/10.1016/j.cub.2021.03.004>

SUMMARY

Anatomical connectivity can constrain both a neural circuit's function and its underlying computation. This principle has been demonstrated for many small, defined neural circuits. For example, connectome reconstructions have informed models for direction selectivity in the vertebrate retina^{1,2} as well as the *Drosophila* visual system.³ In these cases, the circuit in question is relatively compact, well-defined, and has known functions. However, how the connectome constrains global properties of large-scale networks, across multiple brain regions or the entire brain, is incompletely understood. As the availability of partial or complete connectomes expands to more systems and species^{4–8} it becomes critical to understand how this detailed anatomical information can inform our understanding of large-scale circuit function.^{9,10} Here, we use data from the *Drosophila* connectome⁴ in conjunction with whole-brain *in vivo* imaging¹¹ to relate structural and functional connectivity in the central brain. We find a strong relationship between resting-state functional correlations and direct region-to-region structural connectivity. We find that the relationship between structure and function varies across the brain, with some regions displaying a tight correspondence between structural and functional connectivity whereas others, including the mushroom body, are more strongly dependent on indirect connections. Throughout this work, we observe features of structural and functional networks in *Drosophila* that are strikingly similar to those seen in mammalian cortex, including in the human brain. Given the vast anatomical and functional differences between *Drosophila* and mammalian nervous systems, these observations suggest general principles that govern brain structure, function, and the relationship between the two.

RESULTS

To study global properties of brain networks, we focused on connectivity among regions ("mesoscale connectivity"), a scale at which we could both reliably register neural activity signals across individuals and make comparisons to network organization in other systems. To characterize mesoscale connectivity, we established methods for comparing structural and functional connectivity in a common anatomical space. We used data from the *Drosophila* "hemibrain" connectome.⁴ This dataset contains most of the right half of the central brain of a single fly and includes ~25,000 traced cells and ~10 million presynaptic active zones. This connectome has been reconstructed with high accuracy, with over 90% of presynaptic sites (T-bars) assigned to traced neurons (for details of the hemibrain and its reconstruction, see Scheffer et al.⁴). We note that the structural connectivity data in this connectome do not contain information about neuromodulators, the sign of each synapse, or electrical synapses. This connectome also does not include information about many of the connections from the left half of the brain. To measure mesoscale functional connectivity, we used pan-neuronal, *in vivo* calcium imaging of the central brain¹¹ in the absence of explicit sensory stimuli. Each brain ($n = 20$) comprised

~500,000 voxels and was imaged at an isotropic resolution of 3 μm . These voxels were then assigned to anatomical regions based on a template brain atlas. From these measurements, we computed characteristic correlations among brain regions that we refer to as the resting-state functional connectivity. Finally, we compared both structural and functional datasets by registering both into a common anatomical space.^{12,13} We included the central brain regions, with at least half of their volume included in the hemibrain. In total, this analysis includes 37 brain regions that follow the naming convention outlined in Ito et al.¹²

Characterizing structural connectivity

The mesoscale connectivity network is defined by the connection strength between every pair of regions. To measure region-to-region connectivity, we transformed an anatomical brain atlas^{12,14} and synapse locations in the hemibrain to a common brain space (Figure S1; STAR Methods).^{13,15} We used two primary metrics of connection strength (Figures 1A and 1B). First, the cell count connectivity from region A to region B was defined as the total number of neurons with at least one input (post-) synapse in region A and at least one output (pre-) synapse in region B. Second, the T-bar connectivity was defined as the total



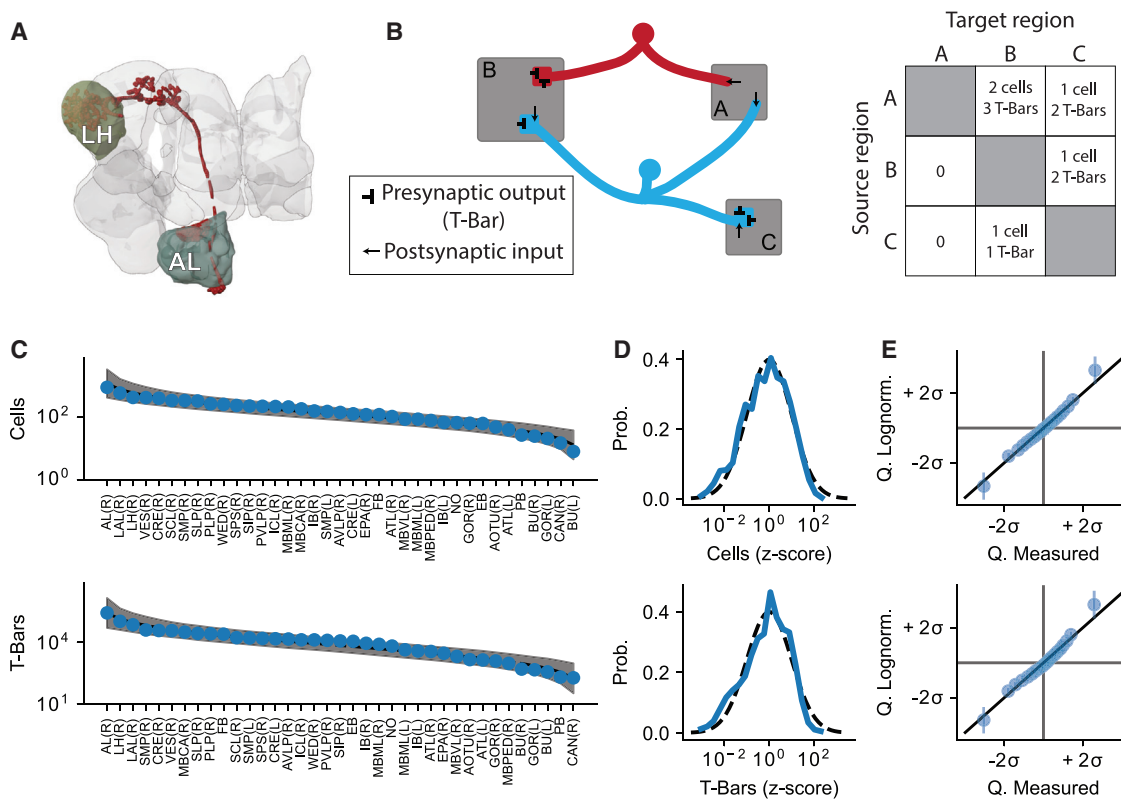


Figure 1. Characterizing mesoscale connectivity using the hemibrain connectome

(A) Portion of the central brain included in the hemibrain connectome used for this analysis, with highlighted example regions. Shown in red is an example of a neuron that projects from the antennal lobe (AL) to the lateral horn (LH).

(B) Schematic showing how inter-region connectivity is quantified. For example, the connection from region A to region B has 2 cells and 3 T-bars.

(C) For an example region (the right AL [AL(R)]), the number of outgoing connections to all regions included in this analysis, ordered from highest to lowest connection strength. Top: inter-region connectivity based on cell count is shown; bottom: inter-region connectivity based on presynaptic T-bars is shown. Data are in blue, and dashed line and shaded region indicate the mean $\pm 2\sigma$ of a log-normal distribution with mean and standard deviation measured from the data.

(D) Inter-region connectivity strength follows a log-normal distribution. Top: outgoing cell count connectivity from each region was Z scored within a region and combined to produce a distribution of connection strengths across all regions (solid blue line). Dashed black line shows, for reference, a log-normal distribution with mean and standard deviation matched to the data. Bottom: same as top but using T-bar count as the connectivity metric is shown.

(E) Top: Q-Q plot to compare the distribution of observed cell count connectivity (horizontal axis) to a best-fitting log-normal distribution (vertical axis); blue points represent mean $\pm 2\sigma$ of matched log-normal distribution quantiles. Bottom: same as top but using T-bar count as the connectivity metric is shown.

number of presynaptic T-bars in region B that belong to a neuron with at least one input in region A.

The outgoing connectivity distributions for each metric are shown for an example region—the right antennal lobe (AL(R)) (Figure 1C). The outgoing connectivity strengths span several orders of magnitude for both the cell count and T-bar metrics. For this example source region, the strongest downstream partners receive several thousand cell connections, whereas the weakest are connected by only a few cells. Interestingly, the outgoing connections closely follow a log-normal distribution of connectivity strengths. A similar pattern was observed for every brain region for both the cell count and T-bar connectivity metrics ($p > 0.05$; Kolmogorov-Smirnov [KS] test against a log-normal distribution for each region in the atlas; Figures 1D and 1E). A similar log-normal distribution of connectivity strengths has been shown for inter-region connectivity in mammalian cortex, including in mouse^{16,17} and monkey.¹⁸

The connectome predicts resting-state functional connectivity

We used whole-brain functional imaging data to measure resting-state correlations among brain regions. We registered our brain volumes to a common anatomical atlas and extracted the average fluorescence signal for each brain region over a period of approximately 25 min (Figure 2B). We then computed the correlation between these signals for each pair of regions (Figure 2C), a measure of their functional connectivity, and averaged these correlations across animals (Figure 2D). Note that the functional correlation values here have been Fisher Z transformed to facilitate estimating statistics across animals. The structural connectivity matrix is shown in Figure 2E, using the cell count connectivity metric (the T-bar connectivity matrix is very similar; $r = 0.86$).

By visual inspection, the functional connectivity in the central brain appears similar to the mesoscale connectivity revealed by the connectome (compare Figures 2D and 2E). To quantify

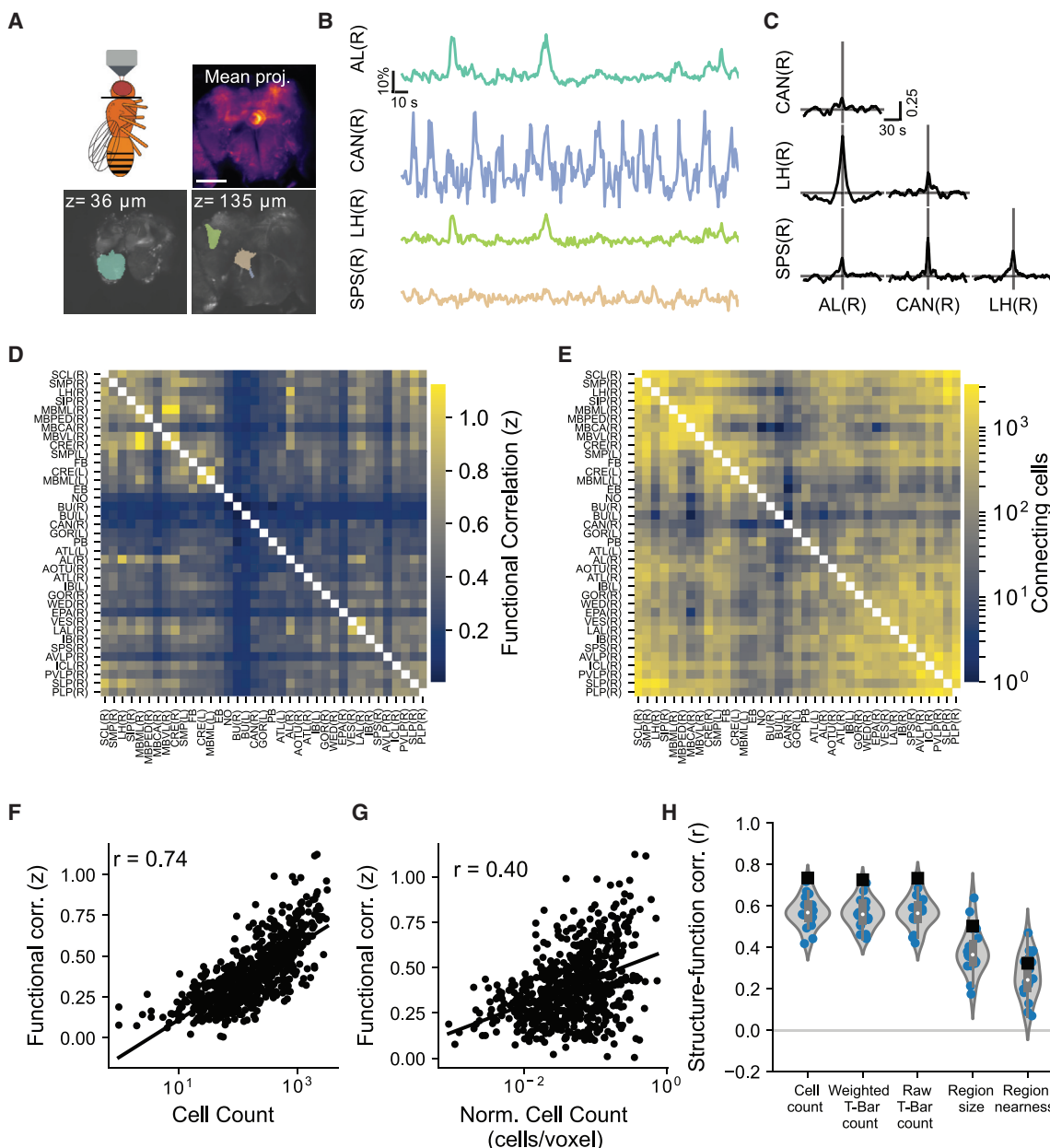


Figure 2. Structural connectivity revealed by the connectome predicts resting-state functional connectivity in the central brain

(A) Overview of functional imaging acquisition. Top left: the central brain is imaged from the anterior of the fly head. Top right: mean projection shows central brain expressing GCaMP6s. Scale bar represents $100 \mu\text{m}$. Bottom: single planes through the central brain show brain regions from an anatomical atlas that has been aligned to *in vivo* data.

(B) Example traces showing GCaMP6s responses of representative brain regions.

(C) Table of cross-correlograms for the pairwise combinations of the four highlighted brain regions in (A) and (B).

(D) Average correlation matrix across $n = 20$ flies; each entry in the matrix is the Fisher transformed correlation value for that pair of regions.

(E) Heatmap showing cell count connectivity between every pair of regions included in this analysis. For both (D) and (E), regions are ordered according to a matrix seriation algorithm based on the structural matrix (STAR Methods).

(F) The log-transformed cell count connectivity between a pair of brain regions is strongly correlated with the functional correlation between those regions. r is the Pearson correlation coefficient.

(G) The cell count connectivity between each pair of regions, normalized by the geometric mean of the region sizes (in voxels), is positively correlated with functional connectivity. r is the Pearson correlation coefficient.

(H) For each anatomical connectivity metric, the distribution of structure-function correlation values for individual flies (blue points and violin plot) and the correlation between structure and the across-animal average functional connectivity matrix (black square).

See also Figures S2 and S3.

this relationship, we plotted the functional correlation between each pair of regions against their structural connectivity (Figure 2F). This analysis reveals a positive correlation between structural and functional connectivity in the central brain (Pearson $r = 0.74$). Because the sizes of these brain regions vary, and larger brain regions tend to contain more cells than smaller regions, we also normalized the cell count connectivity by the number of voxels in each region. This normalized structural connectivity measure was also able to predict functional connectivity (Figure 2G), although to a lesser degree than the raw cell counts. This difference is likely because region size alone can be predictive of functional connectivity (see below).

The connectome contains connectivity information that is not captured by the cell count metric. Does including more-detailed synaptic connectivity increase the correlation between structural and functional connectivity? To address this, we also examined how other mesoscale connectivity metrics predict functional correlations (Figure 2H). In addition to the “cell count” and “T-bar count” connectivity metrics described above, we also examined the “weighted synapse count” as defined in Scheffer et al.⁴—i.e., the T-bar count is weighted by the fraction of postsynapses onto each cell that are within the source region. Surprisingly, the metrics that include information about synapse number are no more predictive of functional connectivity than cell count alone (Figure 2H). We note that the across-animal average functional connectivity (black points in Figure 2H) is higher than the average of individual fly correlations because averaging across animals provides a better estimate of the “true” functional connectivity by averaging out noise in single fly measurements.

Other anatomical features, like the sizes of each region and the physical distance between regions, are significantly correlated with functional connectivity but are less predictive than the connectome-derived metrics (Figure 2H). The correlation between region size or distance and functional connectivity likely reflects the fact that larger regions contain more cells and synapses than smaller regions and that regions that are nearer to one another tend to have stronger anatomical connections (data not shown).

Importantly, we found that the presence of relatively small brain regions did not preclude the accurate estimation of structure-function correlations (Figure S2A). We also found that connectome reconstruction completeness was unrelated to functional connectivity and that reconstruction incompleteness did not result in lower cell count connectivity metrics (Figure S2B). The results of these analyses suggest that these data contain the requisite accuracy to reliably capture mesoscale structure-function relationships.

The brain region atlas used in Figures 1 and 2 contains 37 brain regions within the hemibrain that collectively vary greatly in size. To test whether structural and functional connectivity correspond at a smaller spatial scale, we also measured mesoscale connectivity using a much finer grained segmentation of brain regions.¹⁴ This atlas contains 295 comparably sized segments in the hemibrain, grouped by major brain region. We found a significant correlation between structural and functional connectivity at this finer spatial scale as well (Figure S3). Moreover, the functional connectivity network using this finer grained segmentation was similar to that observed using the coarse atlas (not shown).

Graph features of structural and functional connectivity networks

To further examine correspondences between the structural and functional networks, we used the connectivity matrices in Figure 2 to construct graph representations of each network. In these graphs, each node corresponds to a brain region and each edge corresponds to the connection between two regions.¹⁹ For the structural graph, we symmetrized the connectivity matrix by averaging the outgoing and incoming (i.e., A to B and B to A) connections. Each node of the graph and the top 100 strongest edges of the structural and functional networks are shown in Figures 3A and 3B. The size of each node corresponds to its degree (defined as the sum of the weights across all incoming and outgoing connections associated with that node). Graph features in the structural and functional networks are highly correlated, including the node degree (Figure 3C; Pearson $r = 0.75$) and the node clustering coefficient, which measures how connected a node’s neighbors are (Figure 3D; Pearson $r = 0.76$). However, there are discrepancies between these two graphs, for example, the AVLP(R) has a relatively low degree and clustering coefficient in the functional graph compared to its structural graph. Conversely, regions like the MBML(R) and right lateral horn (LH(R)) have relatively high degrees and clustering coefficients compared to their respective structural graphs. These results suggest that the ability to predict features of functional networks from direct anatomical connections is limited and raises the possibility that indirect connections may also play an important role (Figure 4).

We also investigated whether the structural network shares topological features observed in large-scale networks in the human brain. In particular, we asked whether the mesoscale network shows properties characteristic of (1) a small-world network and (2) a scale-free network. A small-world network is characterized by strong clustering of nodes and relatively short path lengths through the network, even in the absence of dense connections.^{20–22} To determine whether the mesoscale network shows these features, we thresholded the structural connectivity matrix to produce a binary adjacency matrix (Figure 3E, top). We then generated 1,000 random graphs with a connection probability matched to that of the measured adjacency matrix (Figure 3E, bottom). For both the measured graph and the random graphs, we measured the average path length (Figure 3F, top) and clustering coefficient (Figure 3F, bottom). The red vertical line indicates the measured adjacency matrix, and the black distribution shows the computed values for random graphs. As is typical of small-world networks, including connectivity networks in human cortex,²¹ the *Drosophila* structural network has a higher clustering coefficient than equivalent random graphs (23% higher on average) but a similar path length (3% longer on average; see also Scheffer²³). A scale-free network is one in which the distribution of node degree or connection weights follows a power law distribution. This structure has been observed in brain networks, including human functional networks,^{24,25} but see Scheffer²³ and Perin et al.²⁶ The edge weight distribution of the structural network follows a power law decay for intermediate-strength connections but falls off for both very weak edges and for very strong edges (Figure 3G; see Scheffer²³ for a similar analysis on cell-to-cell connectivity). This is consistent with the earlier observation that outgoing connection strengths tend to

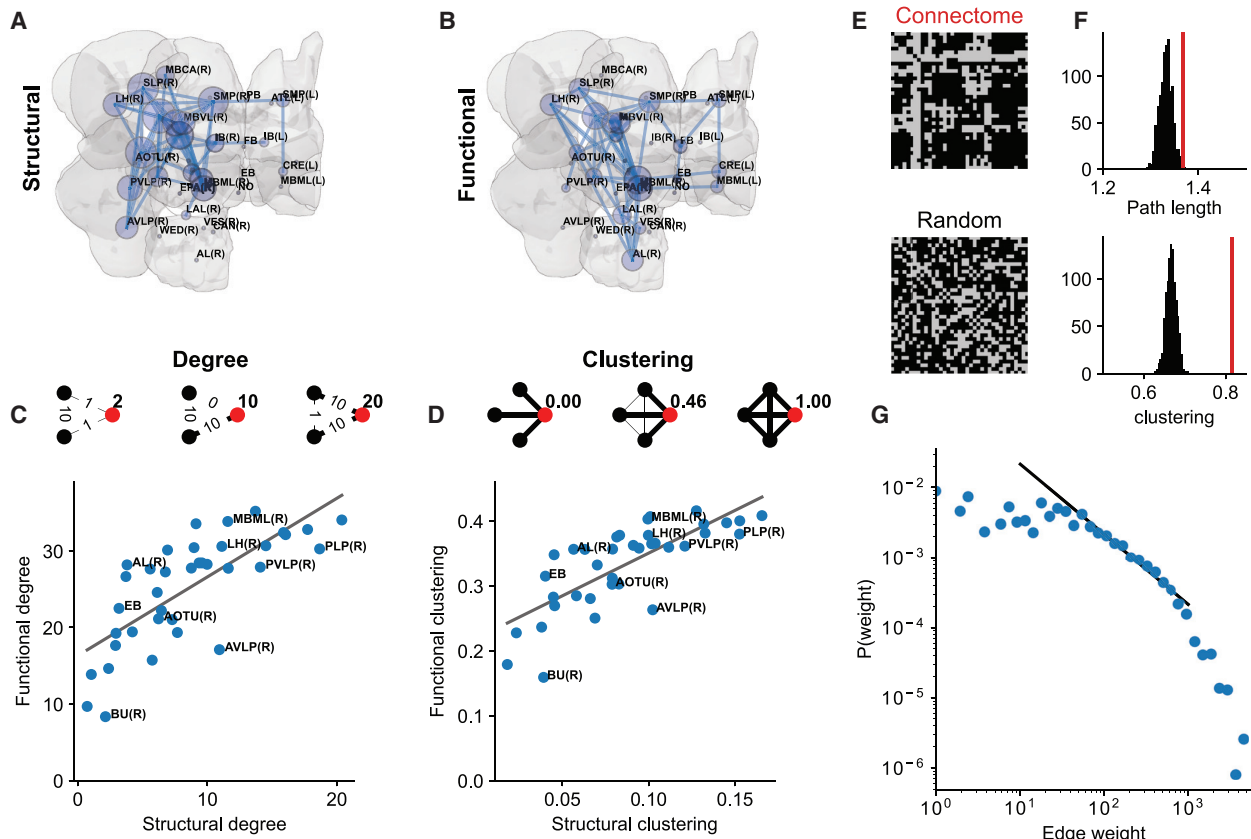


Figure 3. Graph features are shared between structural and functional connectivity networks

(A) Graph representation of the connectome-derived structural network. Each node corresponds to a brain region, and the size of each node represents the degree of that node. The top 100 strongest edges are shown as lines connecting nodes.

(B) Graph representation of the functional network.

(C) Top: schematic illustrating the degree of a node. In each graph example, the degree of the red node is represented by the bold number to its right. A high degree indicates a node with many strong connections (both incoming and outgoing). Bottom: the node degree for the structural graph is correlated to the node degree of the functional graph (Pearson $r = 0.75$).

(D) Top: schematic illustrating the clustering coefficient of a node. A high clustering coefficient indicates a node whose neighbors are highly connected. Bottom: the clustering coefficients in the structural network are correlated to those of the functional network (Pearson $r = 0.76$).

(E) Thresholded structural connectivity matrix and random connectivity matrix with a matched connection probability.

(F) Top: distribution of average path lengths across 1,000 random graphs (black distribution) and average path length for the measured structural graph (red line). Bottom: same as top but for the average graph clustering coefficient is shown.

(G) The distribution of edge weights in the cell-count connectivity network follows a power law distribution for intermediate-strength edge weights only. Black line shows power law scaling, $p \sim w^{-1}$, and blue points are edge weights from the measured structural connectivity.

follow a lognormal distribution (Figure 1), in which the edge weight density falls off steeply at either end of the distribution.

Indirect pathways differentially shape structure-function relationships across the brain

Thus far, we have shown that there is a broad correspondence between structural connectivity and functional correlations. However, there are also discrepancies between functional correlations and what would be predicted based on direct structural connectivity alone (Figure 3). Are these differences between structural and functional connectivity uniformly distributed throughout the brain or are they concentrated in certain regions? To answer this question, we Z scored both the structural and functional connectivity and computed the difference (Figure 4A).

When we averaged the function-structure difference for each region, we found that some brain regions tend to have relatively high functional compared to structural connectivity (Figure 4B). We color coded brain regions by the super-region classification scheme in Ito et al.,¹² where a super-region typically contains regions that are nearby to one another and grouped by anatomical boundaries. This analysis revealed heterogeneity in the function-structure difference across brain regions that in some cases corresponded to membership in a super-region. For example, brain regions belonging to the mushroom body and the LH and AL have a higher average difference than the rest of the regions in the brain ($\alpha < 0.01$; Bonferroni-corrected $p < 0.00125$). The AL and LH are in distinct super-regions but part of a common circuit.^{27–29} On the other hand, regions belonging to the superior neuropils (SNPs), ventromedial

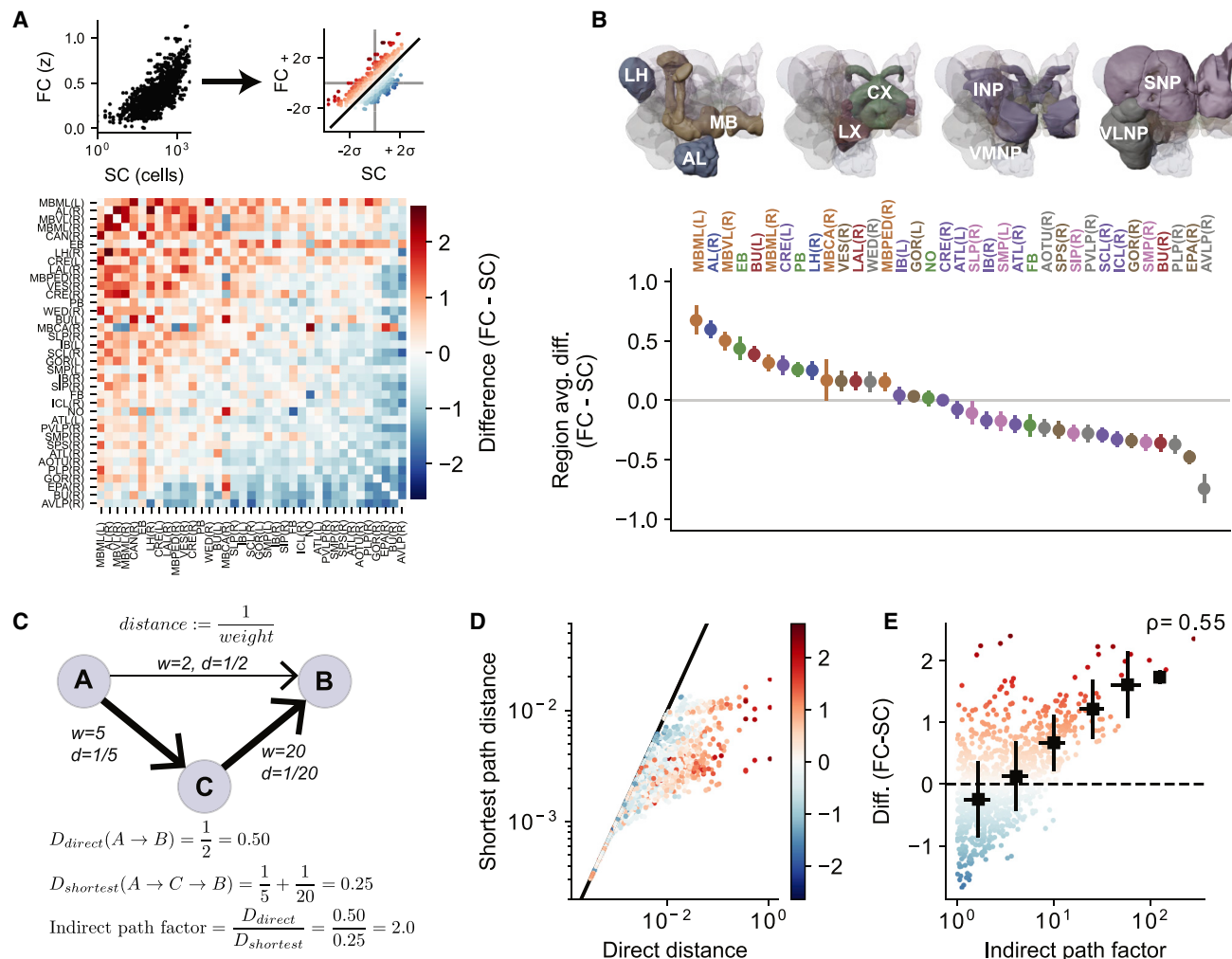


Figure 4. Structure-function relationships in the central brain vary by major brain regions because of indirect connections

(A) Top: we Z scored both structural connectivity (SC) and functional connectivity (FC). Bottom: difference matrix shows, for each pair of regions, the difference between FC and SC. Positive (red) values correspond to region pairs that have relatively high FC given their SC, and negative (blue) values correspond to region pairs that have relatively low FC. Regions have been sorted by the region-average difference in descending order.

(B) FC-SC differences vary across brain super-regions, with the highest differences clustered in the AL/LH and mushroom body regions. Each point corresponds to the mean \pm SEM for that region, across $n = 20$ flies. Points are sorted in descending order of FC-SC difference and colored according to their membership in super-regions, which are illustrated above.

(C) Illustration of direct versus indirect anatomical pathways that could influence functional connectivity. We define the distance between two nodes as the inverse of that edge's weight. To quantify the relative strength of indirect pathways, we define an indirect path factor as the ratio of the direct path distance to the shortest path distance.

(D) For each pair of regions, the shortest path distance is less than or equal to the direct path distance. Points are color coded by the FC-SC difference, as in (A). Note that points further from the line of unity tend to have positive FC-SC differences.

(E) The strength of indirect pathways in the brain accounts for some of the discrepancy between direct pathway structural connectivity and measured functional connectivity. ρ is the Spearman rank order correlation coefficient. Black points represent binned means and SEM.

See also Figure S4.

neuropils (VMNPs), and the ventrolateral neuropils (VLNPs) had relatively low functional connectivity to other regions, given their structural connectivity ($\alpha < 0.01$; Bonferroni-corrected $p < 0.00125$). We also examined structure-function correlation *within* brain regions using the fine-grained brain segmentation and observed a range of intra-region correlations (Figure S3D). Within a region, correlations were typically higher for segments closer together in space.

What might account for the relatively poor prediction of functional connectivity from structural connectivity in these regions? The analysis above uses *direct* anatomical connections between two regions to define their structural connectivity. But many brain networks include strong *indirect* pathways between regions.³⁰ Indeed, this can be a characteristic feature of small-world networks (Figure 3).^{21,22} One important consequence of the impact of indirect pathways is that two brain regions may

be functionally correlated despite having a weak (or nonexistent) direct connection between them, as multi-synaptic connections could produce correlated neural activity.

To measure the presence of indirect pathways in the inter-region structural network, we first defined the distance between two regions as the inverse of the connectivity weight between them (Figure 4C). Therefore, a pair of regions with a strong connection between them will be separated by a short distance. For each pair of brain regions, A and B, we computed the direct distance, $D_{\text{direct}}(A,B)$, which is the distance of the direct pathway between regions A and B. We also computed the shortest path distance, $D_{\text{shortest}}(A,B)$, between regions A and B using Dijkstra's algorithm.³¹ This commonly used algorithm finds the single shortest path between any two nodes in a (connected) graph. Note that the direct and shortest path distances are not necessarily symmetric (i.e., the distance from A to B can be different than the distance from B to A). Because of this, we used a directed graph to represent the structural network. This approach can reveal multi-step, indirect connections between a pair of regions that are stronger than the direct connection between them. Thus, for every pair of regions, the shortest path distance is always less than or equal to the direct distance (Figure 4D). This analysis shows that connections with higher-than-expected functional connectivity tend to have much longer direct path distances compared to their shortest paths. To quantify this, we defined an indirect path factor, which is the ratio of the direct path distance to the shortest path distance. An indirect path factor of 1.0 indicates a connection where the shortest path is equal in distance to the direct path, and values greater than 1.0 indicate a shortest path that is shorter than the direct path. In this way, the indirect path factor quantifies the relative strength of the primary indirect pathway between a pair of regions. We found that the strength of indirect pathways was positively correlated with the function-structure difference (Spearman's rank correlation $\rho = 0.55$). A similar result is seen for the finer grained brain segmentation (Spearman's $\rho = 0.41$; data not shown). This means that regions that showed higher functional connectivity than predicted from direct structural connectivity tend to be connected to other regions by strong indirect pathways.

To further test whether indirect pathways contribute to functional connectivity, we fit linear regression models to predict functional connectivity based on different measures of structural connectivity. We found that a model that included both shortest path distance and direct connectivity outperformed a model that included only direct distance (cell count metric: $r^2 = 0.60$ versus $r^2 = 0.53$ for the direct connectivity only model; T-bars metric: $r^2 = 0.59$ versus $r^2 = 0.52$ for the direct connectivity only model; Figure S4). Taken together, these results suggest that indirect anatomical pathways in the brain exert an important influence on functional connectivity, especially for regions like the mushroom body, AL, and LH.

DISCUSSION

Previous work looking at specific circuits, for example, in the mushroom body^{32,33} and central complex,³⁴ described relationships between connectome structure and circuit function. The release of a nearly complete central brain connectome combined with the ability to measure whole-brain functional activity

in defined brain regions has allowed us to, for the first time, relate synapse-level structural connectivity to mesoscale functional connectivity both within and across brain regions.^{4,11} We found that cell-level anatomical connectivity provides a strong constraint on resting-state functional connectivity (Figure 2), with over half of the variance in functional correlations being accounted for by the variance in the number of cells that connect two regions (Figure S4).

Although the direct, inter-region structural connectivity was broadly predictive of functional correlations, we found that indirect pathways could also contribute significantly to functional connectivity (Figure 4). Indirect pathways are thought to be important in many circuits,^{9,35} including in human cortex.³⁶ Indirect connections are especially important for some brain regions in particular, including the mushroom body, which is associated with multisensory integration and learning,³⁷ suggesting that dense, indirect connectedness might be important for these computations. Conversely, brain regions in the SNP, VMNP, and VLNP showed strong structural connectedness to other regions compared to their functional connectivity (Figure 4). The structural connectivity among these regions may support activity patterns not explored in the fly's resting state, and other behavioral states or stimulation conditions may reveal different functional connectivity for regions like these.

We used one metric of indirect connections between two regions, namely the shortest path distance, but one could imagine other indirect paths also contributing to functional connectivity in a meaningful way. Indeed, recent work developed a graph-embedding procedure to predict functional connectivity from structural connectivity in the human brain,^{36,38} which allows for the influence of higher order interactions in general. We suspect that, rather than the specific shortest path being of particular importance in shaping functional connectivity between a pair of regions, the shortest path distance is a proxy for more-general indirect path connectedness. Disentangling which higher order interactions most strongly shape functional connectivity will be an important task in future work.

An illuminating approach to understanding large-scale structure-function relationships in the brain has emerged in human neuroscience, where macro-scale structural connectivity patterns can be related to functional connectivity using noninvasive imaging or electrical recording techniques (for reviews, see Bullmore and Sporns³⁹ and Suárez et al.⁴⁰). Several of these studies have shown that functional connectivity can be predicted by structural connectivity to some degree.^{40–43} The structure-function correlation we found in the *Drosophila* central brain is higher than typically reported in macro-scale networks in the human brain, where MRI-based structural and functional connectivity is similarly positively correlated but generally with lower correlation coefficients (for review, see Suárez et al.⁴⁰).⁴² There are many factors that could contribute to this difference, including different levels of temporal and spatial precision in the functional measurements, vastly different amounts of biological detail in the structural connectivity measurements, and/or genuine biological differences between the two systems. Interestingly, the inclusion of detailed synaptic information (i.e., the number of synapses associated with a given inter-region connection) did not increase the correlation between structural and functional connectivity (Figure 2). This suggests that synapse-level connectivity does

not much constrain functional connectivity at the mesoscale level, despite synapse count being very important for smaller, functionally defined circuits.^{3,44} Mesoscale functional correlations reflect the influence of many neurons that individually belong to different functional circuits. Although these individual neurons can vary substantially in their synapse number, when averaging over large brain regions, the overall synapse count connectivity is highly correlated with the cell count connectivity ($r = 0.86$; data not shown).

In addition to the general correspondence between structural and functional connectivity, we found a number of other intriguing similarities between *Drosophila* central brain networks and networks in mammalian cerebral cortex. For example, we found that the structural network in the *Drosophila* central brain showed signs characteristic of a small-world network (Figure 3), which has been shown before in human structural and functional networks.^{21,22} We also found that inter-region connectivity strengths are log-normally distributed (Figure 1), which is also the case in mouse^{16,17} and monkey¹⁸ cortex. The observation that brain networks with such different biological and anatomical features share a key network topology suggests a deep correspondence in either developmental rules and/or functional constraints. It is not unusual for biological variables to be log-normally distributed. Indeed, multiplicative interactions among many variables will tend to produce log-normally distributed variables.^{45,46} In the context of nervous system development, interactions between pre- and postsynaptic cells that are shaped by cooperative combinations of adhesion and signaling molecules will be multiplicative. We speculate that the shared features between fly and vertebrate brains that can be observed at the mesoscale are the result of these universal phenomena at the microscale.

STAR★METHODS

Detailed methods are provided in the online version of this paper and include the following:

- KEY RESOURCES TABLE
- RESOURCE AVAILABILITY
 - Lead contact
 - Materials availability
 - Data and code availability
- EXPERIMENTAL MODEL AND SUBJECT DETAILS
- METHOD DETAILS
 - Whole brain imaging to measure functional connectivity in the central brain
- QUANTIFICATION AND STATISTICAL ANALYSIS
 - Analysis of connectome data to characterize inter-region structural connectivity
 - Statistical analyses and graph methods

SUPPLEMENTAL INFORMATION

Supplemental information can be found online at <https://doi.org/10.1016/j.cub.2021.03.004>.

ACKNOWLEDGMENTS

We thank Estela Stephenson for technical support and members of the Clanin lab for feedback on the work and on this manuscript. This work was

supported by NIH grants F32-MH118707 (M.H.T.) and RO1-EY022638 (T.R.C.) and a grant from the Simons Foundation (T.R.C.).

AUTHOR CONTRIBUTIONS

M.H.T. and K.M. conceived the project. K.M. performed all the functional imaging experiments and registered *in vivo* data to the *Drosophila* brain atlas. M.H.T. analyzed functional connectivity data and structural connectivity data from the connectome, performed analyses, and generated the figures. M.H.T., K.M., and T.R.C. wrote the manuscript. T.R.C. supervised all aspects of the work.

DECLARATION OF INTERESTS

The authors declare no competing interests.

Received: December 22, 2020

Revised: February 8, 2021

Accepted: March 1, 2021

Published: March 25, 2021

REFERENCES

1. Helmstaedter, M., Briggman, K.L., Turaga, S.C., Jain, V., Seung, H.S., and Denk, W. (2013). Connectomic reconstruction of the inner plexiform layer in the mouse retina. *Nature* **500**, 168–174.
2. Kim, J.S., Greene, M.J., Zlateski, A., Lee, K., Richardson, M., Turaga, S.C., Purcaro, M., Balkam, M., Robinson, A., Behabadi, B.F., et al.; EyeWires (2014). Space-time wiring specificity supports direction selectivity in the retina. *Nature* **509**, 331–336.
3. Takemura, S.Y., Nern, A., Chklovskii, D.B., Scheffer, L.K., Rubin, G.M., and Meinertzhagen, I.A. (2017). The comprehensive connectome of a neural substrate for ‘ON’ motion detection in *Drosophila*. *eLife* **6**, e24394.
4. Scheffer, L.K., Xu, C.S., Januszewski, M., Lu, Z., Takemura, S.Y., Hayworth, K.J., Huang, G.B., Shinomiya, K., Maitlin-Shepard, J., Berg, S., et al. (2020). A connectome and analysis of the adult *Drosophila* central brain. *eLife* **9**, e57443.
5. Cook, S.J., Jarrell, T.A., Brittin, C.A., Wang, Y., Bloniarz, A.E., Yakovlev, M.A., Nguyen, K.C.Q., Tang, L.T.-H., Bayer, E.A., Duerr, J.S., et al. (2019). Whole-animal connectomes of both *Caenorhabditis elegans* sexes. *Nature* **571**, 63–71.
6. Kasthuri, N., Hayworth, K.J., Berger, D.R., Schalek, R.L., Conchello, J.A., Knowles-Barley, S., Lee, D., Vázquez-Reina, A., Kaynig, V., Jones, T.R., et al. (2015). Saturated reconstruction of a volume of neocortex. *Cell* **162**, 648–661.
7. Markram, H., Müller, E., Ramaswamy, S., Reimann, M.W., Abdellah, M., Sanchez, C.A., Ailamaki, A., Alonso-Nanclares, L., Antille, N., Arsever, S., et al. (2015). Reconstruction and simulation of neocortical microcircuitry. *Cell* **163**, 456–492.
8. Abbott, L.F., Bock, D.D., Callaway, E.M., Denk, W., Dulac, C., Fairhall, A.L., Fiete, I., Harris, K.M., Helmstaedter, M., Jain, V., et al. (2020). The mind of a mouse. *Cell* **182**, 1372–1376.
9. Bargmann, C.I., and Marder, E. (2013). From the connectome to brain function. *Nat. Methods* **10**, 483–490.
10. Meinertzhagen, I.A. (2018). Of what use is connectomics? A personal perspective on the *Drosophila* connectome. *J. Exp. Biol.* **221**, jeb164954.
11. Mann, K., Gallen, C.L., and Clandinin, T.R. (2017). Whole-brain calcium imaging reveals an intrinsic functional network in *Drosophila*. *Curr. Biol.* **27**, 2389–2396.e4.
12. Ito, K., Shinomiya, K., Ito, M., Armstrong, J.D., Boyan, G., Hartenstein, V., Harzsch, S., Heisenberg, M., Horberg, U., Jenett, A., et al.; Insect Brain Name Working Group (2014). A systematic nomenclature for the insect brain. *Neuron* **81**, 755–765.
13. Bogovic, J.A., Otsuna, H., Heinrich, L., Ito, M., Jeter, J., Meissner, G., Nern, A., Colonell, J., Malkesman, O., Ito, K., and Saalfeld, S. (2020). An

- unbiased template of the *Drosophila* brain and ventral nerve cord. *PLoS ONE* 15, e0236495.
14. Robie, A.A., Hirokawa, J., Edwards, A.W., Umayam, L.A., Lee, A., Phillips, M.L., Card, G.M., Korff, W., Rubin, G.M., Simpson, J.H., et al. (2017). Mapping the neural substrates of behavior. *Cell* 170, 393–406.e28.
 15. Bates, A.S., Manton, J.D., Jagannathan, S.R., Costa, M., Schlegel, P., Rohlfing, T., and Jefferis, G.S. (2020). The natverse, a versatile toolbox for combining and analysing neuroanatomical data. *eLife* 9, e53350.
 16. Oh, S.W., Harris, J.A., Ng, L., Winslow, B., Cain, N., Mihalas, S., Wang, Q., Lau, C., Kuan, L., Henry, A.M., et al. (2014). A mesoscale connectome of the mouse brain. *Nature* 508, 207–214.
 17. Wang, Q., Sporns, O., and Burkhalter, A. (2012). Network analysis of corticocortical connections reveals ventral and dorsal processing streams in mouse visual cortex. *J. Neurosci.* 32, 4386–4399.
 18. Markov, N.T., Ercsey-Ravasz, M.M., Ribeiro Gomes, A.R., Lamy, C., Magrou, L., Vezoli, J., Misery, P., Falchier, A., Quilodran, R., Gariel, M.A., et al. (2014). A weighted and directed interareal connectivity matrix for macaque cerebral cortex. *Cereb. Cortex* 24, 17–36.
 19. Bassett, D.S., Zurn, P., and Gold, J.I. (2018). On the nature and use of models in network neuroscience. *Nat. Rev. Neurosci.* 19, 566–578.
 20. Bassett, D.S., and Bullmore, E. (2006). Small-world brain networks. *Neuroscientist* 12, 512–523.
 21. Sporns, O., and Zwi, J.D. (2004). The small world of the cerebral cortex. *Neuroinformatics* 2, 145–162.
 22. Sporns, O., Chialvo, D.R., Kaiser, M., and Hilgetag, C.C. (2004). Organization, development and function of complex brain networks. *Trends Cogn. Sci.* 8, 418–425.
 23. Scheffer, L.K. (2020). Graph properties of the adult *Drosophila* central brain. *bioRxiv*. <https://doi.org/10.1101/2020.05.18.102061>.
 24. Eguíluz, V.M., Chialvo, D.R., Cecchi, G.A., Baliki, M., and Apkarian, A.V. (2005). Scale-free brain functional networks. *Phys. Rev. Lett.* 94, 018102.
 25. Bullmore, E.T., and Bassett, D.S. (2011). Brain graphs: graphical models of the human brain connectome. *Annu. Rev. Clin. Psychol.* 7, 113–140.
 26. Perin, R., Berger, T.K., and Markram, H. (2011). A synaptic organizing principle for cortical neuronal groups. *Proc. Natl. Acad. Sci. USA* 108, 5419–5424.
 27. Masse, N.Y., Turner, G.C., and Jefferis, G.S.X.E. (2009). Olfactory information processing in *Drosophila*. *Curr. Biol.* 19, R700–R713.
 28. Schultzhaus, J.N., Saleem, S., Iftikhar, H., and Carney, G.E. (2017). The role of the *Drosophila* lateral horn in olfactory information processing and behavioral response. *J. Insect Physiol.* 98, 29–37.
 29. Wilson, R.I. (2013). Early olfactory processing in *Drosophila*: mechanisms and principles. *Annu. Rev. Neurosci.* 36, 217–241.
 30. Avena-Koenigsberger, A., Misic, B., and Sporns, O. (2017). Communication dynamics in complex brain networks. *Nat. Rev. Neurosci.* 19, 17–33.
 31. Dijkstra, E.W. (1959). A note on two problems in connexion with graphs. *Numer. Math.* 1, 269–271.
 32. Eichler, K., Li, F., Litwin-Kumar, A., Park, Y., Andrade, I., Schneider-Mizell, C.M., Saumweber, T., Huser, A., Eschbach, C., Gerber, B., et al. (2017). The complete connectome of a learning and memory centre in an insect brain. *Nature* 548, 175–182.
 33. Li, F., Lindsey, J.W., Marin, E.C., Otto, N., Dreher, M., Dempsey, G., Stark, I., Bates, A.S., Pleijzier, M.W., Schlegel, P., et al. (2020). The connectome of the adult *Drosophila* mushroom body provides insights into function. *eLife* 9, e62576.
 34. Hulse, B.K., Haberkern, H., Franconville, R., Turner-Evans, D.B., Takemura, S., Wolff, T., Noorman, M., Dreher, M., Dan, C., Parekh, R., et al. (2020). A connectome of the *Drosophila* central complex reveals network motifs suitable for flexible navigation and context-dependent action selection. *bioRxiv*. <https://doi.org/10.1101/2020.12.08.413955>.
 35. Marder, E. (2015). Understanding brains: details, intuition, and big data. *PLoS Biol.* 13, e1002147.
 36. Rosenthal, G., Vásá, F., Griffa, A., Hagmann, P., Amico, E., Goñi, J., Avián, G., and Sporns, O. (2018). Mapping higher-order relations between brain structure and function with embedded vector representations of connectomes. *Nat. Commun.* 9, 2178.
 37. Yagi, R., Mabuchi, Y., Mizunami, M., and Tanaka, N.K. (2016). Convergence of multimodal sensory pathways to the mushroom body calyx in *Drosophila melanogaster*. *Sci. Rep.* 6, 29481.
 38. Grover, A., and Leskovec, J. (2016). node2vec: scalable feature learning for networks. *arXiv*, arXiv:1607.00653v1. <https://arxiv.org/abs/1607.00653>.
 39. Bullmore, E., and Sporns, O. (2009). Complex brain networks: graph theoretical analysis of structural and functional systems. *Nat. Rev. Neurosci.* 10, 186–198.
 40. Suárez, L.E., Markello, R.D., Betzel, R.F., and Misic, B. (2020). Linking structure and function in macroscale brain networks. *Trends Cogn. Sci.* 24, 302–315.
 41. Honey, C.J., Kötter, R., Breakspear, M., and Sporns, O. (2007). Network structure of cerebral cortex shapes functional connectivity on multiple time scales. *Proc. Natl. Acad. Sci. USA* 104, 10240–10245.
 42. Honey, C.J., Sporns, O., Cammoun, L., Gigandet, X., Thiran, J.P., Meuli, R., and Hagmann, P. (2009). Predicting human resting-state functional connectivity from structural connectivity. *Proc. Natl. Acad. Sci. USA* 106, 2035–2040.
 43. Hermundstad, A.M., Bassett, D.S., Brown, K.S., Aminoff, E.M., Clewett, D., Freeman, S., Frithsen, A., Johnson, A., Tipper, C.M., Miller, M.B., et al. (2013). Structural foundations of resting-state and task-based functional connectivity in the human brain. *Proc. Natl. Acad. Sci. USA* 110, 6169–6174.
 44. Takemura, S.Y., Aso, Y., Hige, T., Wong, A., Lu, Z., Xu, C.S., Rivlin, P.K., Hess, H., Zhao, T., Parag, T., et al. (2017). A connectome of a learning and memory center in the adult *Drosophila* brain. *eLife* 6, e26975.
 45. Limpert, E., Stahel, W.A., and Abbt, M. (2001). Log-normal distributions across the sciences: keys and clues: on the charms of statistics, and how mechanical models resembling gambling machines offer a link to a handy way to characterize log-normal distributions, which can provide deeper insight into variability and probability—normal or log-normal: that is the question. *BioScience* 51, 341–352.
 46. Buzsáki, G., and Mizuseki, K. (2014). The log-dynamic brain: how skewed distributions affect network operations. *Nat. Rev. Neurosci.* 15, 264–278.
 47. Hagberg, A., Swart, P., and Schult, D.S. (2008). Exploring network structure, dynamics, and function using networkx. <https://www.osti.gov/servlets/purl/960616>.
 48. Cachero, S., Ostrovsky, A.D., Yu, J.Y., Dickson, B.J., and Jefferis, G.S.X.E. (2010). Sexual dimorphism in the fly brain. *Curr. Biol.* 20, 1589–1601.

STAR★METHODS

KEY RESOURCES TABLE

REAGENT or RESOURCE	SOURCE	IDENTIFIER
Deposited data		
Functional data and derived structural connectivity	This paper	https://doi.org/10.6084/m9.figshare.13349282
Transformation from JFRC2 -> JRC2018F template brain space	This paper	https://doi.org/10.6084/m9.figshare.13349282
Janelia Hemibrain Connectome	Scheffer et al. ⁴	https://www.janelia.org/project-team/flyem/hemibrain
Experimental models: Organisms/strains		
w[1118]; P{y[+t7.7] w[+mC] = GMR57C10-GAL4}attP2	https://bdsc.indiana.edu	RRID: BDSC_39171
w[1118]; P{y[+t7.7] w[+mC] = 20XUAS-IVS-GCaMP6s}attP40	https://bdsc.indiana.edu	RRID: BDSC_42746
w[*]; P{y[+t7.7] w[+mC] = 10XUAS-IVS-myR::tdTomato}attP40	https://bdsc.indiana.edu	RRID: BDSC_32222
Software and algorithms		
Custom analysis code	This paper	https://github.com/mturner/SC-FC
NetworkX	Hagberg et al. ⁴⁷	https://networkx.org/
Blender	Blender Foundation	https://www.blender.org/
Python3.6	Python Software Foundation	https://www.python.org/
Seriate v1.1.2	https://pypi.org/user/srcd/	https://pypi.org/project/seriate/
Natverse	Bates et al. ¹⁵	http://natverse.org/
Computational Morphometry Toolkit (CMTK)	NITRC	https://www.nitrc.org/projects/cmtk/

RESOURCE AVAILABILITY

Lead contact

Requests for resources and information not made available here should be directed to and will be fulfilled by the Lead Contact, Max Turner (mturner@stanford.edu).

Materials availability

This study did not generate new unique reagents.

Data and code availability

All analysis code can be accessed at <https://github.com/mturner/SC-FC>. Data from the hemibrain connectome (v1.2)⁴ was accessed using the Python neuPrint bindings as well as the R natverse package neuprintr (see **Key resources table**). Original data have been deposited to figshare (<https://doi.org/10.6084/m9.figshare.13349282>).

EXPERIMENTAL MODEL AND SUBJECT DETAILS

Imaging flies expressed GCaMP6s and myR::tdTomato pan-neuronally, and were of the following genotype:

$$\frac{w^+}{w^-}; \frac{UAS - myr :: tdTomato}{UAS - GCaMP6s}; \frac{nSyb - Gal4}{+}$$

Flies were raised on molasses medium at 25°C with a 12/12 hr light/dark cycle. Flies were housed in mixed male/female vials and 5-day old females were selected for imaging.

METHOD DETAILS

Whole brain imaging to measure functional connectivity in the central brain

Details of whole brain imaging can be seen in Mann et al.¹¹ For imaging, flies were immobilized and their central brain exposed from the anterior of the head. Imaging experiments were performed on a resonant scanning two photon microscope (Bruker) equipped

with a piezo Z drive which allows for fast volumetric acquisition. High resolution anatomical scans are taken at a resolution of $0.6 \times 0.6 \times 1 \mu\text{m}$, as well as high speed functional scans at $3 \mu\text{m}$ isotropic spatial resolution and a temporal sampling frequency of 1.2 Hz. Anatomical scans are used to register to a common brain atlas, which is then used to extract time series data from each brain region.

QUANTIFICATION AND STATISTICAL ANALYSIS

Analysis of connectome data to characterize inter-region structural connectivity

All data and statistical analyses, modeling, and plot generation was performed using custom-written Python and R code (see [Data and code availability](#) above). In order to compare structural and functional connectivity, we registered each to the JRC2018F template brain space.¹³ We used CMTK to transform the two brain segmentations used here (the coarse “Ito Atlas”¹², and finer “Bran-son Atlas”¹⁴) from their native JFRC2 template brain space into JRC2018F template brain space.⁴⁸ The transformation from JFRC2 to JRC2018F space is included in the accompanying data. We then used the natverse & neuprintR to transform synapse locations in the hemibrain to JRC2018F template space and compute which brain region each synapse belongs to. We tested alignment between hemibrain coordinates and the Ito brain atlas by (1) visual inspection and (2) by selecting some neuron types with known, restricted synapse locations and examining the correspondence to synapse densities in the hemibrain database ([Figure S1](#)).

To measure structural connectivity from a source region, A to a target region, B, we used one of several connectivity metrics. (1) The primary metric used in the main text is the cell count connectivity metric. In this case, the connectivity weight from region A to B is defined as the total number of neurons that have at least one input synapse in region A and at least one output synapse (i.e., a pre-synaptic T-Bar) in region B. (2) A secondary metric we used was the T-Bar connectivity metric. In this case, we summed the number of T-Bars in region B that are associated with connecting cells from A (as defined in the cell count metric above). (3) The weighted synapse count is a metric defined in Scheffer et al.⁴ This metric weights each connecting cell’s T-Bar count in region B by the fraction of total input synapses to that cell that are in region A.

To compare each region’s outgoing connectivity distribution to a log-normal distribution, we constructed a log-normal distribution for each region, based on that region’s mean and standard deviation connection weight. We then drew 1000 randomly-generated distributions (each with $n = 37$, as in the data) from this fit model and compared this population of random distributions to the data using a Kolmogorov-Smirnov (KS) test. To combine distributions across regions, we first z-scored the log-transformed distribution for each region. This allows for different regions to have different means and standard deviations, but tests that they each follow their own log-normal distribution.

Statistical analyses and graph methods

We high-pass filtered each region-average fluorescence signal using a Butterworth filter with a cutoff frequency of 0.01 Hz to remove very slow drift in the fluorescence intensity. For display ([Figure 2](#)) we converted each region response to a dF/F measurement relative to a baseline fluorescence defined as the mean fluorescence over the entire imaging session. To compute functional connectivity between a pair of regions, we used the Pearson linear correlation coefficient, r , between their two response traces. This is equivalent to the $\delta t = 0$ amplitude in the cross-correlograms shown in [Figure 2](#). To facilitate comparison across animals as well as to the structural connectivity, we Fisher Z-transformed each inter-region correlation coefficient ([Equation 1](#)).

$$z = \operatorname{arctanh}(r) \quad (\text{Equation 1})$$

The functional connectivity matrix shown in [Figure 2](#) represents the average z-transformed correlation matrix across $n = 20$ animals, but a connectivity matrix from an individual animal is also robustly correlated to the structural connectivity in the connectome ([Figure 2H](#)). We ordered both the structural and functional connectivity matrices according to a traveling salesperson seriation algorithm ([Key resources table](#)).

To compare structural and functional connectivity ([Figure 2F](#)), we first symmetrized the structural connectivity matrix by adding its own transpose to itself and dividing by 2. The functional connectivity matrix, by definition, is already symmetric. We then compared the upper triangle of the functional connectivity matrix to the upper triangle of the symmetrized structural connectivity matrix.

To compare graph features between the structural and functional networks, we used NetworkX⁴⁷ to create a graph for each network using its associated connectivity matrix. For the graph displays and analysis in [Figure 3](#), we first normalized each connectivity matrix by the maximum edge weight in the matrix. To compare the structural network to a matched random graph, we generated a binary adjacency matrix by applying a threshold to the structural connectivity matrix. We chose a threshold value of 35% of the maximum edge weight. For low threshold values, nearly every possible edge is realized and consequently little small world structure is observed. For higher threshold values, the graph is no longer fully connected.

For the difference analysis in [Figure 4](#), we z-scored both the functional connectivity values as well as the (log-transformed) structural, cell-count connectivity values. This approach allowed us to better compare the structural and functional connectivity strength for a given connection, at least in relation to their respective connectivity distributions. We grouped brain regions by the *Drosophila* central brain super-region definitions in Ito et al.¹²

To perform the shortest path analysis in [Figure 4](#), we first defined the distance (D) for each connection as the inverse of that connection's weight (W; [Equation 2](#)).

$$D(A, B) = \frac{1}{W(A, B)} \quad (\text{Equation 2})$$

Using this distance definition, we used the Dijkstra's Shortest Path First algorithm³¹ in NetworkX to compute the shortest path between each pair of brain regions.

Supplemental Information

**The connectome predicts resting-state functional
connectivity across the *Drosophila* brain**

Maxwell H. Turner, Kevin Mann, and Thomas R. Clandinin

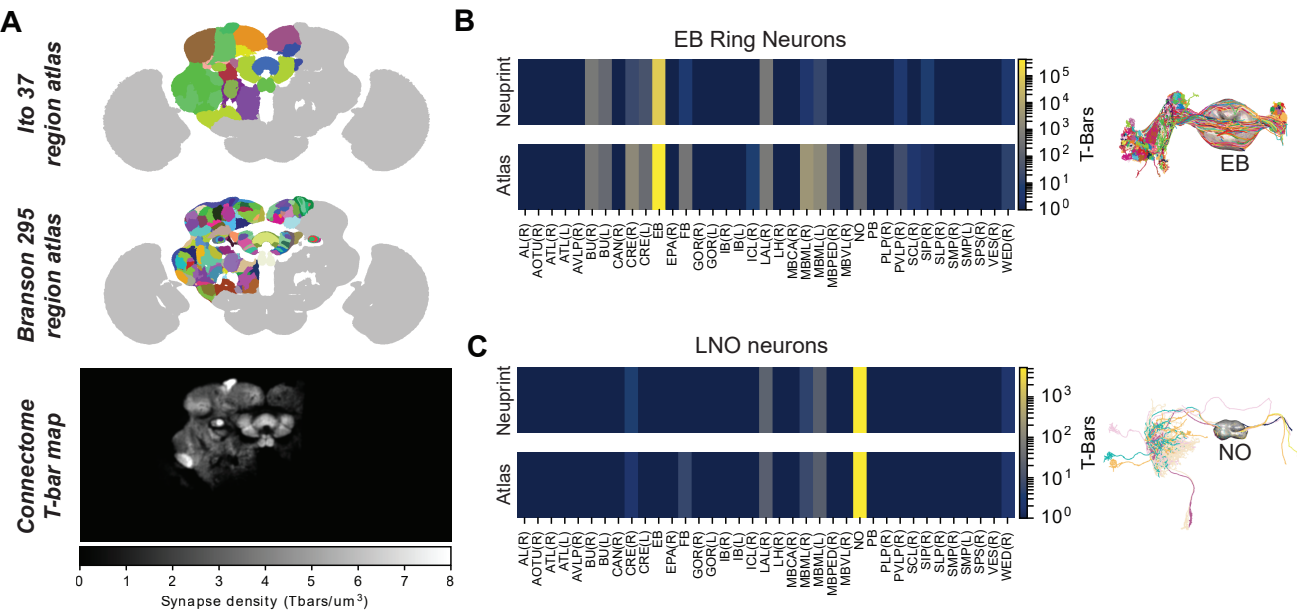


Figure S1: Alignment of brain atlas and hemibrain connectome. Related to STAR methods.

(A) We used two brain atlases, each transformed to JRC2018F template brain space¹³ to define brain regions in these analyses. Top: 37 regions from the Ito atlas¹², middle: 295 regions from the Branson segmentation atlas¹⁴. Bottom: T-bar density measured in the hemibrain connectome and transformed to JRC2018F template brain space showing overlap between neuropil in the transformed hemibrain space and the transformed atlases. Note that the synapse density mask has been Gaussian-smoothed for visualization.

(B) To further test registration between our atlases and the hemibrain synapse locations, we selected ellipsoid body (EB) ring neurons as a test case. Most of these neurons' T-Bars reside in the EB, as seen in the brain region tags in the Neuprint hemibrain database (top heatmap). Our transformations and comparison in the common JRC2018F brain space reveal a very similar pattern of T-Bar density ($r > 0.99$). Note the log color scale for T-Bar density. (C) same as (B) for LNO neurons, which have most of their T-Bars in the Nodulus (NO), which is the smallest region in our atlas, and therefore the most sensitive to errors in alignment (correlation between atlas alignment method and neuprint region tags: $r > 0.99$.)

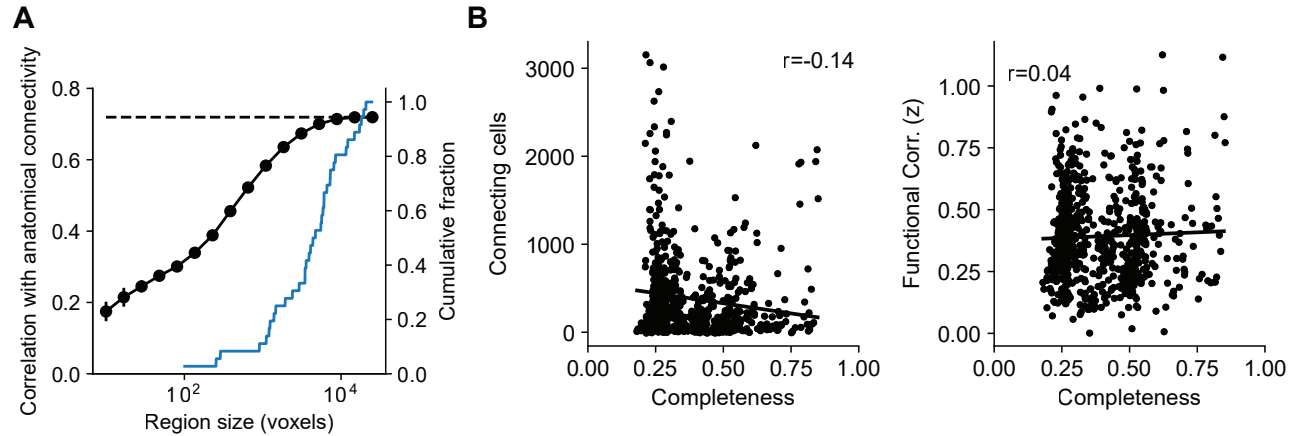


Figure S2: Region size and reconstruction completeness does not preclude accurate measurement of structure function correlations. Related to Figure 2. (A) To assess whether relatively lower signal-to-noise in smaller brain regions limited our ability to infer functional connectivity and its correlation with structural connectivity, we performed a subsampling analysis. We randomly subsampled each region by the number of voxels indicated on the horizontal axis and measured structure-function correlations for each subsampled functional connectivity matrix. When only ~ 100 voxels are included in each region, the estimated structure-function correlation is only ~ 0.30 , when up to ~ 1000 voxels are included in each region the estimated structure-function correlation is ~ 0.60 . For comparison, the right axis shows the cumulative histogram of region sizes. The subsampled structure-function correlation is approximately 90% of the full estimate at the 25th percentile of region size, indicating that most of the regions are considerably larger than the sizes that interfere with the estimate of the functional connectivity. (B) To understand the effect of the connectome reconstruction completeness on our estimates of structural connectivity, we computed a “completeness score” for each pair of brain regions, which was defined as the fraction of cell-assigned T-Bars in the source region multiplied by the fraction of cell-assigned postsynapses in the target region. Left: Higher completeness scores do not indicate stronger cell count connectivity, likely because this measure of connectivity is not sensitive to precise synapse numbers. Right: Higher completeness scores are not related to functional connectivity.

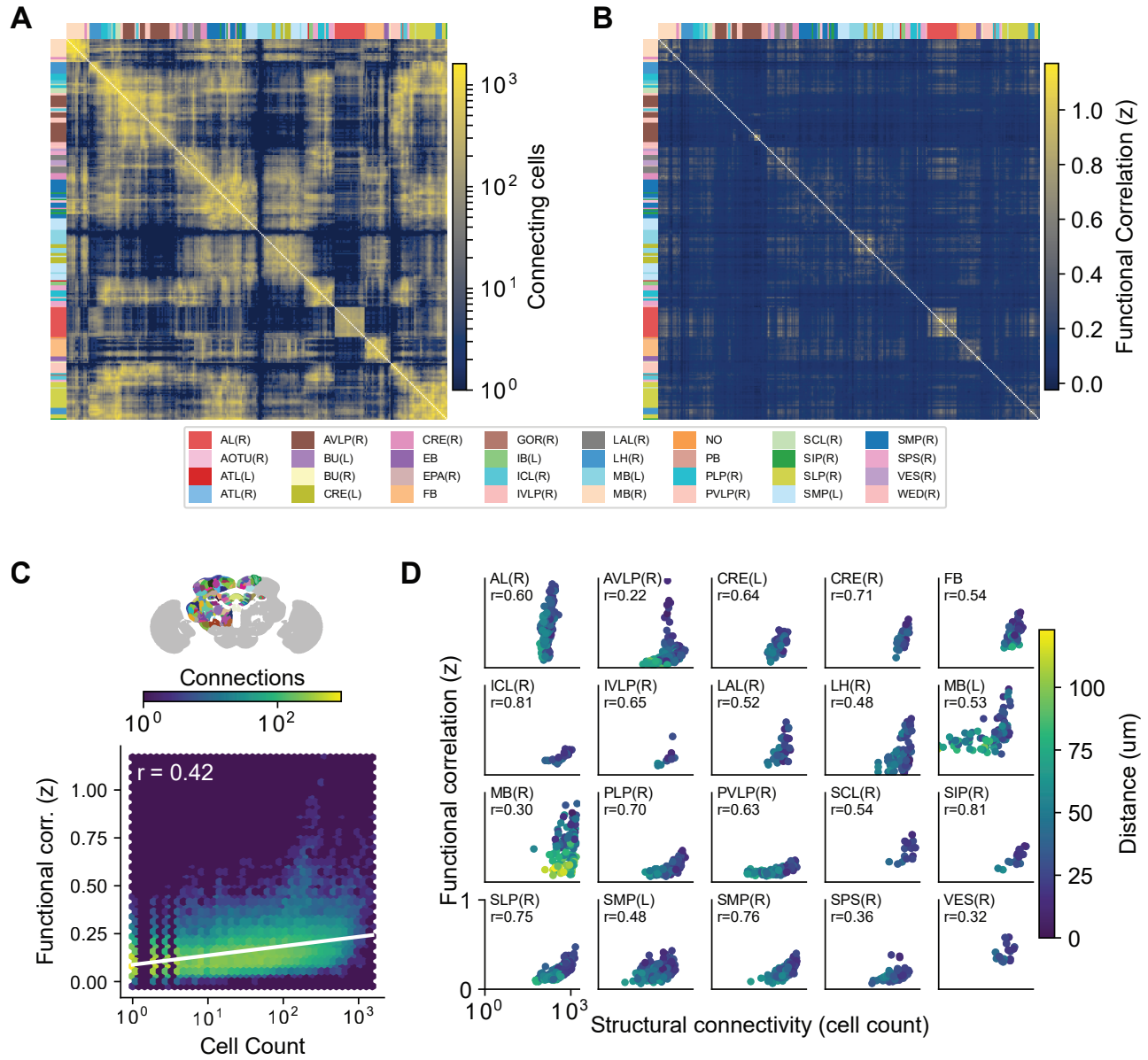


Figure S3: Structure-function correlation with a fine-grained brain atlas. Related to Figure 2. (A) Structural connectivity matrix for the 295 Branson segmentation atlas regions included in this analysis. Regions are color-coded and ordered according to a seriation algorithm as in Figure 2. (B) functional connectivity matrix for the same brain regions. (C) Functional connectivity in the fine-grained atlas is predicted by structural connectivity. Data are shown as a joint distribution because of the large number of connections to display. Note that the banding pattern on the left side of the plot is due to the log scaling. (D) Intra-region structural and functional connectivity is shown for all brain regions with more than 3 brain segments. Structural and functional connectivity are correlated within every brain region, and there is variability in the strength of this relationship across brain regions. Colors show region-to-region distance, showing that nearby segments within a region are more likely to be highly correlated and structurally connected.

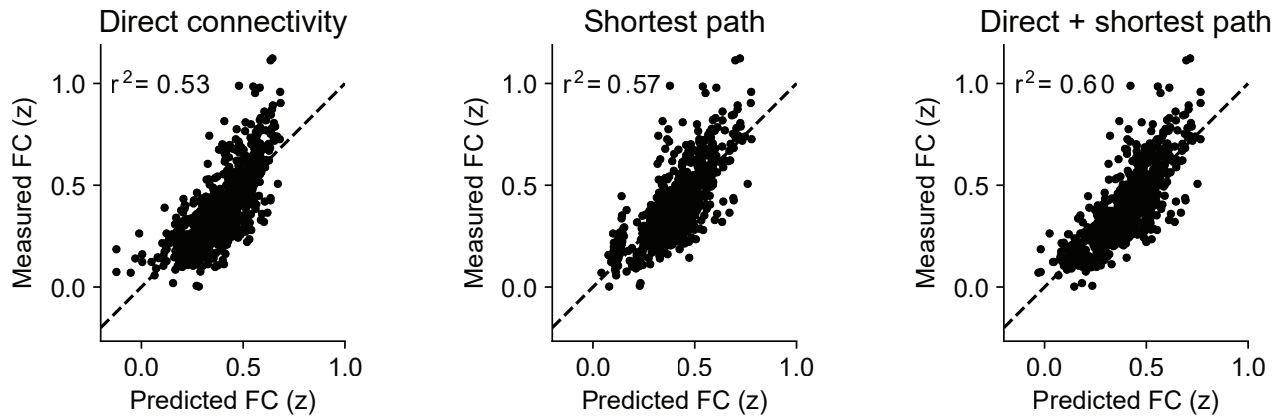
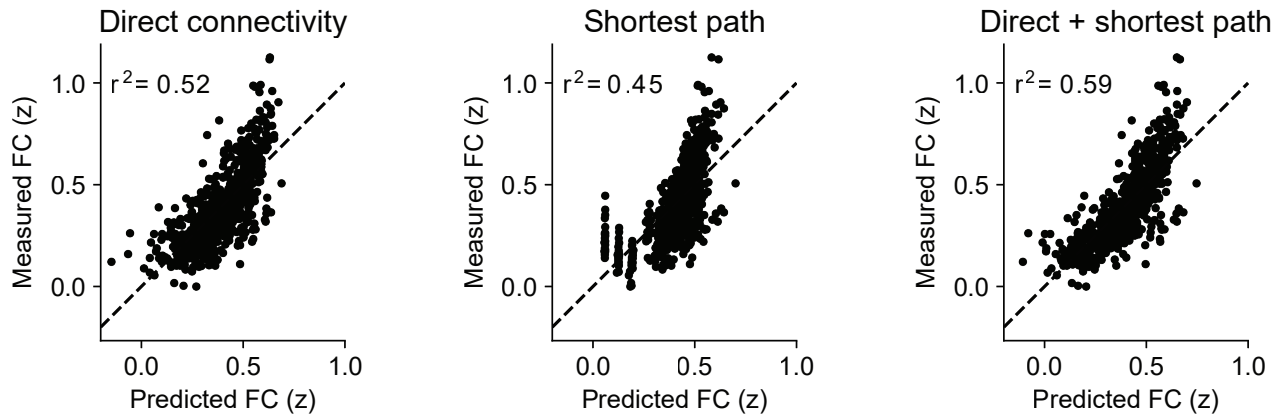
A**Connectivity metric: Cell count****B****Connectivity metric: T-Bar count**

Figure S4: Linear regression models can account for over half of the variance in functional correlations using structural connectivity. Related to Figure 4. (A) Using the cell-count connectivity metric, we fit three linear regression models to predict measured functional correlations based on: (i) Direct region-to-region connectivity (left); (ii) shortest path distance between each pair of regions (middle); and (iii) both direct connectivity and shortest path distance (right). For each model, the fraction of explained variance (r^2), measured using 10-fold cross validation, is shown. (B) Same as (A) but using the T-Bar count connectivity metric instead of cell count connectivity.